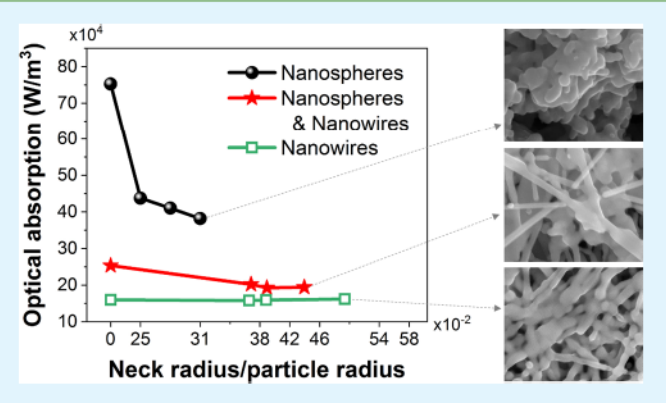


Hyun-Jun Hwang and Rajiv Malhotra*

Department of Mechanical and Aerospace Engineering, Rutgers University, 98 Brett Road, Piscataway, New Jersey 08854, United States

Supporting Information

ABSTRACT: Concurrently reducing processing temperature, electrical resistance, and material cost with scalable fabrication capabilities is critical for conductive elements of flexible and planar electronics. Intense pulsed light sintering (IPL) of mixed dissimilar-shape conductive nanostructures may achieve this goal. However, this potential is hindered by knowledge gaps on how dissimilarity in nanostructure shape affects interparticle neck growth kinetics in general and the self-damping coupling between neck growth and optical absorption in IPL. We study these phenomena for IPL of mixed Ag nanowires (NWs, 40 nm diameter, 100-200 µm length) and nanospheres (NSs, 40 nm diameter), both experimentally and by linking molecular dynamics simulations with optical modeling. An optimal



50:50 mixing ratio lowers resistivity (5.59 μΩ·cm) and peak temperatures (250-150 °C) relative to pure NS films and reduces material costs relative to pure NW films with similar resistivity, in 2.5 s of IPL. The drop in peak temperatures in consecutive optical pulses reduces with greater NW content. Sintering-induced dislocation generation drives higher neck growth at NW-NS and NW-NW interfaces and anisotropic neck growth at NW-NS interfaces. This indicates that when NWs are introduced into NS films, along with lesser number of interfacial contact points, an inherent reduction in sintering-induced junction resistivity plays a major role in reducing film resistivity. The self-damping coupling and optical absorption, which drive temperature evolution in IPL, are tunable by nanostructure shape. The introduction of NWs into a NS ensemble reduces the dependence of optical absorption on neck growth. We discuss how these insights elucidate a set of physical phenomena that can guide the choice of dissimilar shaped nanostructures to concurrently reduce resistivity and temperatures in IPL and other sintering processes.

KEYWORDS: nanowires, nanoparticles, sintering, temperature, conductivity, self-damping

1. INTRODUCTION

Silver (Ag) nanostructures are widely used as conductive elements in printed flexible and planar electronics due to their oxidation resistance, good dispersibility in water for ink fabrication, and their low electrical resistivity. 1-4 The fabrication of printed circuits from such nanostructures for applications such as energy storage,⁵ solar cells,^{6,7} transistors,⁸ and antennas⁹ on substrates such as paper,¹⁰ fabric,¹¹ and thermally sensitive polymers¹² has significant economic impact.¹³ In a typical fabrication process, the printed Ag nanostructures are sintered to fuse them into a contiguous conductive structure. Simultaneously reducing sintering temperatures, electrical resistance, material costs, and processing time is a key requirement for such sintering processes. Among the various extant sintering methods, the inherently high scalability of the intense pulsed light sintering (IPL) process has generated significant interest in the community. 14-24 IPL sintering was first introduced in 2004 through patents by Seiko Epson Corporation (JP2004-277832A and JP2004-39846A). They suggested employing IPL to sinter

metal nanoparticles. The first demonstration of IPL to sinter nanomaterials on polymer substrates was reported in 2009 by Kim et al., 25 triggering enormous interest in the field of the printed electronics. Since then, numerous studies on the structural reformation and chemical modification of metallic, carbon-based, and semiconductor nanomaterials using IPL have been reported.

IPL uses high-energy pulsed visible light (power spectrum in Supporting Information Figure S1) to sinter nanostructures in seconds. Localized plasmonic absorption by Ag nanostructures during IPL obviates direct heating of the bulk of the substrate, and the large optical footprint (e.g., ≥ 1 ft x 1 in. possible in this work) enables high throughput.²⁴ However, the peak IPL temperatures needed to achieve low resistivity after sintering are still quite high for the typically used Ag nanosphere (NS) films and patterns (e.g., ≈ 250 °C for 20 nm diameter Ag²⁰).

Received: October 9, 2018 Accepted: December 26, 2018 Published: December 26, 2018

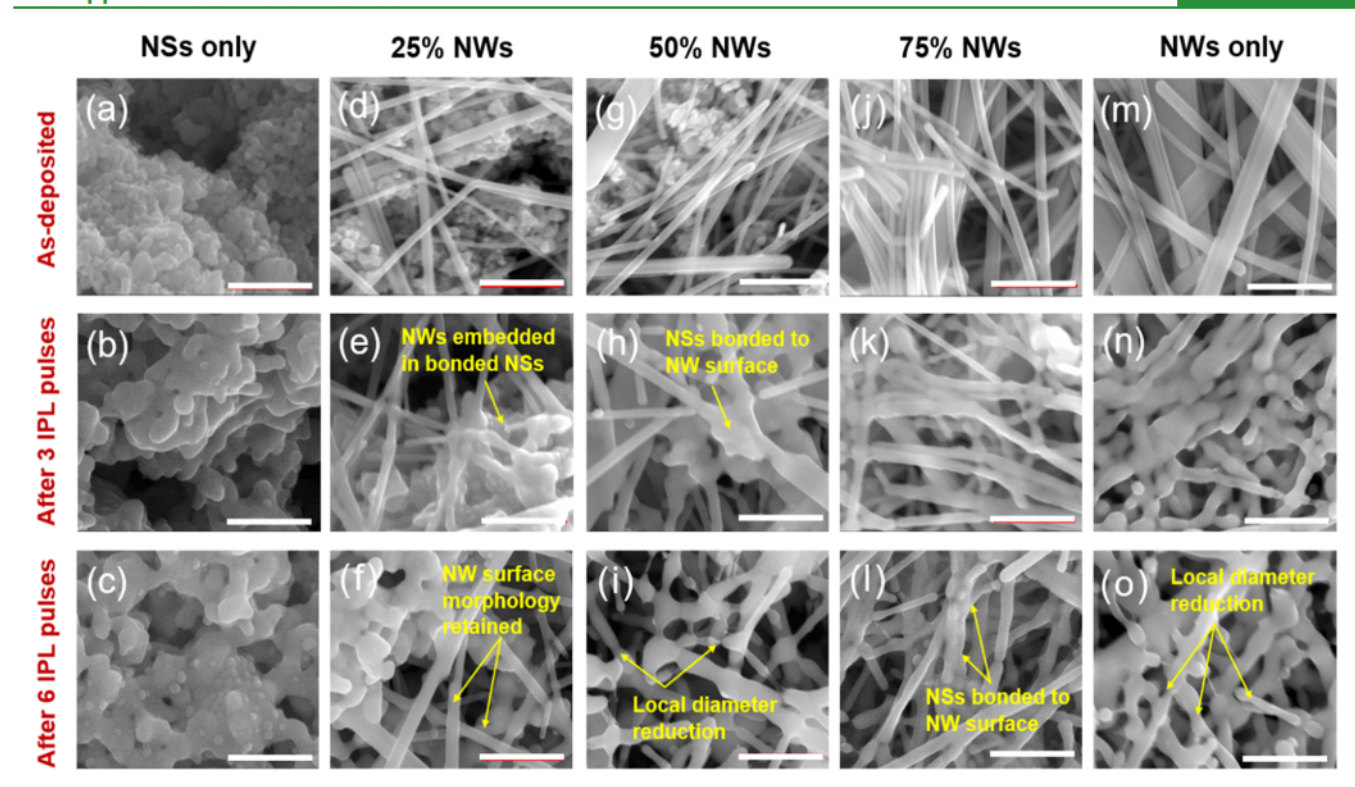


Figure 1. SEM images of unsintered and post-IPL films for (a-c) NS-only film; (d-f) 25% NW content film; (g-i) 50% NW content film; (j-l) 75% NW content film; (m-o) NW-only film. Scale bar corresponds to 500 nm length.

This necessitates small and expensive NSs to enable lower temperature sintering or expensive thermally resistant substrates like polyimide to tolerate the higher temperatures.

In recent work, IPL sintering of mixed nanowires (NWs) and NSs²⁶ showed the potential to achieve lower resistivity, similar to observations in isothermal sintering.²⁷ However, the IPL temperatures were not reported. Further, the NW length was small (comparable to the NS diameter), and much lower resistivity is achievable with higher aspect-ratio NWs.²⁸ In isothermal sintering, the inclusion of NWs into a NS ensemble was posited to reduce postsintered conductivity by reducing number of interparticle contact points.²⁷ This may be thought to be the sole reason for reduced resistivity in the IPL of mixed NWs and NSs. However, the use of mixed NW-NS structures can influence temperatures and resistivity in IPL in the following nontrivial ways. First, nanostructure shape can affect the neck growth kinetics and therefore the junction resistivity and film conductivity.²⁹ For example, NW-NS and NS-NS interfaces may have different neck growth rates since the surface area to volume ratios are different.³⁰ Although there is significant knowledge of NS-NS sintering,³¹⁻³⁴ there is little work on quantifying the neck growth kinetics and mechanisms at NW-NS and NW-NW interfaces. Second, unlike isothermal oven sintering the temperature in IPL changes dynamically with evolution of neck growth between nanostructures. Plasmonic absorption during IPL increases the ensemble temperature, and the resultant temperature-driven neck growth reduces the sharpness of nanoscale features between adjacent nanostructures. This creates a negative feedback on further optical absorption and thus reduces additional temperature rise and interparticle neck growth, i.e., a self-damping coupling. 15,19,35 This self-damping coupling manifests as a reduction in peak temperatures in consecutive IPL pulses. The significance of controlling this self-damping coupling is appreciated by noting that the degree of sintering depends on achieving high enough temperature to overcome the activation energy for mass transfer and on sustaining this temperature (or higher) for a long enough time for significant mass transfer. Past work has modeled optical absorption in sintered NW-only¹⁵ and mixed NW-NS³⁵ ensembles. These works assumed purely shrinkage-based neck growth, which was constant at all nanostructure interface types, an assumption that is shown to be erroneous in this work and thus could not capture the effects of interface-specific neck growth on self-damping in IPL sintering.

To simultaneously control temperature and resistivity in IPL, there is a need to bridge the above knowledge gaps. This study answers the following questions (1) How does the neck growth kinetics for NW-NS and NW-NW interfaces compare to NS-NS interfaces and what neck growth mechanisms govern this comparison? (2) How does the introduction of NWs into a NS ensemble affect self-damping behavior in IPL, when interface-specific neck growth kinetics are considered? Our IPL experiments show that the introduction of NWs into a NS ensemble reduces peak sintering temperatures while achieving higher conductivity but also uncovers a limit beyond which no added advantage is obtained by adding additional NWs. Our molecular dynamics (MD) simulations of sintering show unexpected trends in interface-specific neck growth and anisotropic neck growth at NW-NS interfaces. The mass transfer mechanisms that are responsible for these observations are elucidated. Electromagnetic simulations of the sintered nanostructure ensembles show that addition of NWs into a NS ensemble inherently affects self-damping and absorption efficiency in IPL. To the best of our knowledge, this is the first study that combines experiments, MD simulations, and electromagnetic simulations to reveal these previously unknown phenomena. The insights

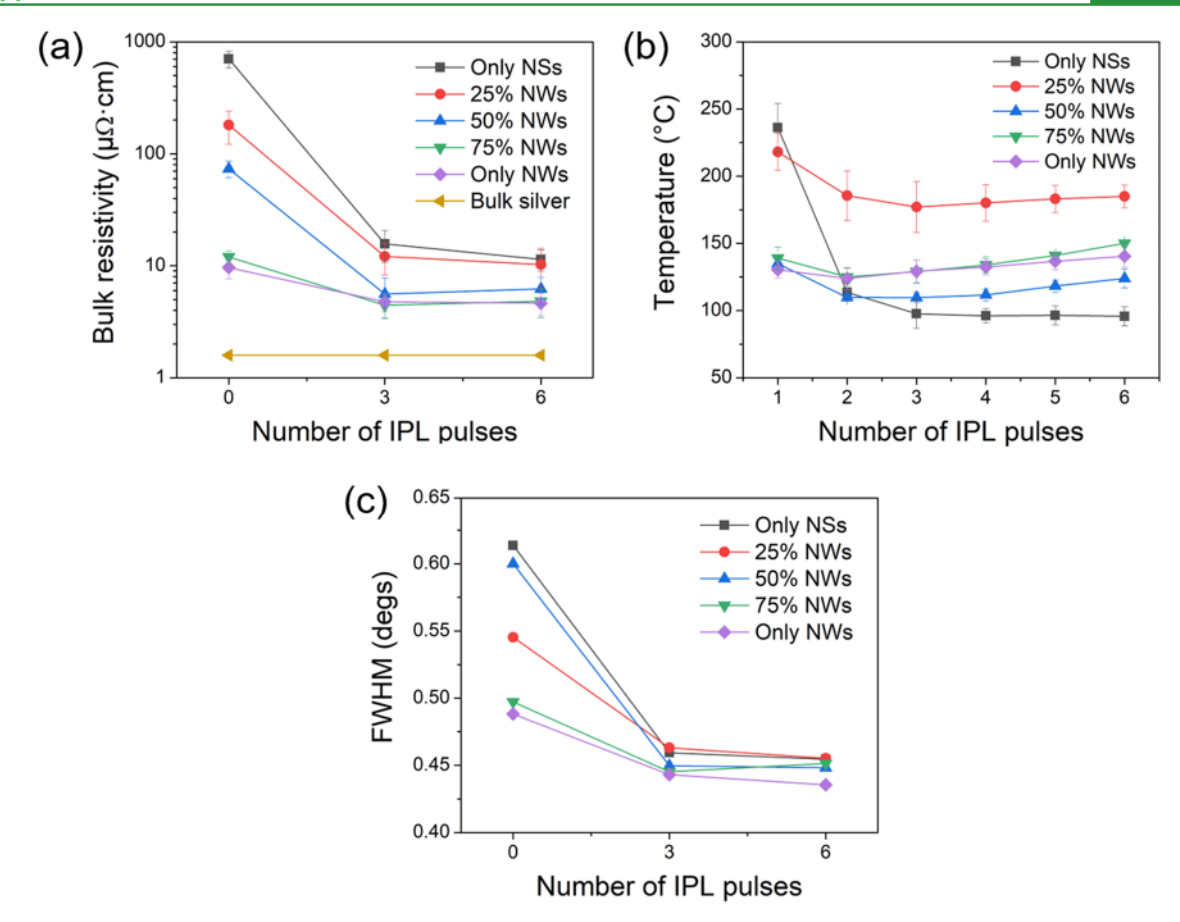


Figure 2. (a) Change in film resistivity due to IPL. (b) Peak pulse temperature as a function of nanowire content. (c) Full width at half maximum (FWHM) of the (111) peak from X-ray diffraction (XRD) spectra. 0 pulse indicates as-deposited and dried film.

gained provide a set of physical considerations to guide the choice of mixed-shape nanostructures in IPL, even beyond NWs and NSs, for further reductions in temperature and resistivity.

2. RESULTS AND DISCUSSION

2.1. Temperature and Morphology Evolution in IPL Experiments. Ag NSs (nominal diameter 40 nm, US Research Nanomaterials) and NWs (nominal diameter 40 nm and length 100-200 μ m, ACS Materials) were suspended in ethanol and deposited on glass substrate as films of similar thickness (Table S1), using a wide-area aerosol spray system. Typically, nanostructures of diameter smaller than 10 nm are more expensive, and most work in IPL has used larger nanostructure diameters. 14-24 Thus, nanostructures with diameter greater than 10 nm were used here. The NW/NS ratio by weight was varied from 0 to 100% in 25% increments (Table S1), and the total weight percentage of silver in all of the inks was constant. IPL was performed using a pulsed linear xenon lamp (Sinteron 3000, Xenon Corp.). The lamp on time and incident fluence were fixed at 1275 μ s and 20 J/cm², respectively, for 3 and 6 consecutive optical pulses. Additional details on IPL procedure and characterization methods are provided in the Methods section and in our previous work.³⁵

Scanning electron microscopy (SEM) images of the films, in Figure 1, show post-IPL neck growth between the nanostructures for all NW/NS ratios. For the unsintered films, the smooth axial surface of the NWs results in sharp nanoscale features at the less numerous NW-NW interfaces (Figure 1m)

in contrast to the more numerous NS-NW (Figure 1d,g,j) and NS-NS (Figure 1a) interfaces in other mixing ratios. For the postsintered NS-only film, neck growth between NSs results in more contiguous structures that exhibit a significant increase in the nanoscale feature size in the film (Figure 1a-c). For a 25% NW content film (e.g., Figure 1d-f), the NWs get embedded into a bed of surrounding NSs after IPL but do not lose their axial surface morphology. As the NW content increases further (Figure 1g-o), the postsintered morphology again shows neck growth but with retention of axial surface morphology of the NWs. Overall, the increase in nanoscale feature size in the postsintered film is lesser for increasing NW content.

Figure 2a shows that the resistivity of the as-deposited films (dried at 70 °C, i.e., 0 pulses) reduces by nearly 2 orders of magnitude with increase in NW content. This agrees with past work²⁷ and occurs because NWs provide more contiguous pathways with lesser interparticle contacts for electron percolation. After 3 pulses (2.5 s), the films with NW/NS ratio of 50:50 achieve a resistivity of 9.5-11 $\mu\Omega$ ·cm (6-7.5 times that of bulk silver) and lie within 1 error of the resistivity for 75:25 ratio films and pure NW films. The highest temperature for all of the mixing ratios is in the first pulse (Figure 2b). This first pulse temperature for pure NS films is about 250 °C, similar to that in previous work, 20 and decreases with increasing NW content (Figures 2b and S2). This is because the total optical absorption in the unsintered state reduces with increasing NW content (Figure S3) due to reduction in number of sharp nanoscale interfaces that can plasmonically absorb light, as seen from SEM images in Figure

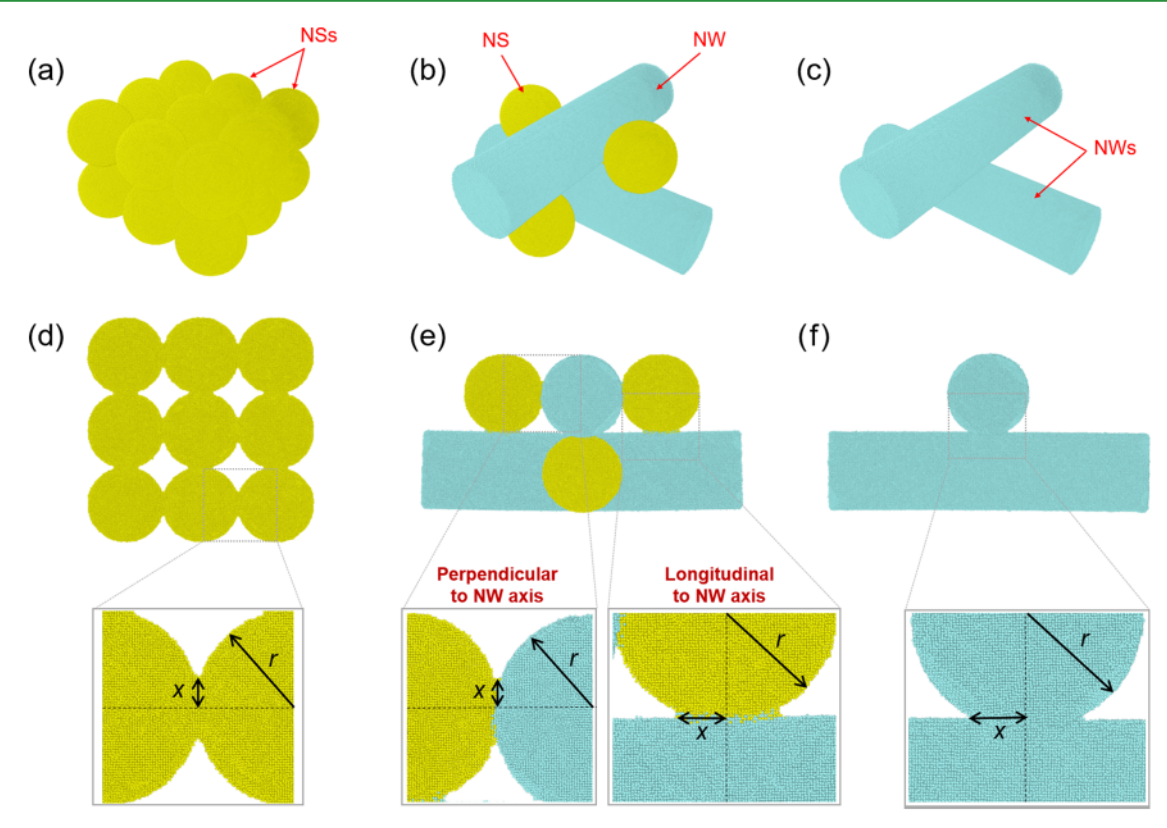


Figure 3. Ensemble configurations for MD simulations (a) NS-only, (b) mixed NW-NS ensemble, (c) NW-only. (d-f) Side views of the ensembles after sintering at 900 K. Inset figures show necks between the nanostructures. Here, we denote neck radius as x and NS/NW radius as r.

1. The 50:50 mixing ratio enables significant reduction in maximum processing temperature to around 150 °C as compared to NS-only films (around 250 °C), and adding further NWs gives no additional reduction in the maximum temperature. Since NWs are significantly more expensive than NSs, a NW/NS ratio of 50:50 is therefore optimal for achieving similar resistivity at lower costs than a pure NW film while significantly reducing temperatures relative to a NS-only film.

For all of the mixing ratios, the peak pulse temperature drops after the first pulse (Figure 2b) and levels off after 3 pulses (within 1 error) due to a significant reduction in optical absorption upon sintering (Figure S3). This drop in optical absorption is the key driver for change in peak pulse temperature with number of pulses. This results in minimal change in crystallite size (leveling off in full width at half maximum (FWHM) from X-ray diffraction (XRD) spectra, Figure 2c) and in resistivity (Figure 2a) after 3 pulses. The SEM images (Figure 1) also show that the morphology does not change as significantly from 3 to 6 pulses, as it does from as-deposited film to 3 pulses. This evolution of temperature and morphology is a characteristic consequence of selfdamping coupling in IPL20 and indicates that the optical absorption is too low after 3 pulses to cause any additional neck growth in the film.

Figure 2b also yields important observations on evolution of film temperature during IPL. For the NS-only film, there is a very sharp drop in temperature (\approx 60%) within 3 pulses, with the majority of the drop occurring in the second pulse. For 25% NW content, the temperature in the first pulse is similar to that of the NS-only film, but the drop in temperature in subsequent pulses is significantly lesser (\approx 15%). For even

greater NW content, the drop in temperature reduces progressively (7-8% drop for 50 and 75% NW content) till for the pure NW case the pulse peak temperatures are constant within 1 error. In essence, the drop in temperature in consecutive pulses progressively reduces with increasing NW content. This is due to the relatively lesser reduction in optical absorption from unsintered film to the 3-pulse sintered film, as the NW content increases (Figure S3). The source of this difference in postsintered optical behavior may be from the film morphology. Since the post-IPL increase in nanoscale feature size is mitigated with increasing NW content (Figure 1) and smaller nanoscale feature size typically results in higher absorption efficiency, 36 the change in absorption upon IPL also reduces with greater NW content. These observations point to a potential inherent dependence of self-damping coupling on shape mixing. However, the sintering-induced change in the nanoscale feature size depends significantly on the degree of neck growth at NS-NS, NW-NS, and NW-NW interfaces. In our experiments, the significant differences in temperature evolution cause different neck growth for different mixing ratios, as seen from the FWHM trends (Figure 2c). Thus, our experiments cannot justify the above claim of shape-dependent self-damping by themselves since they cannot conclusively assess the independent impact of mixing NWs and NSs on selfdamping behavior and neck growth kinetics. The results from the MD simulations and electromagnetic modeling are used to resolve this issue.

3.2. Neck Growth Kinetics. MD simulations of isothermal sintering at 500, 700, and 900 K for 300 ps were performed within the embedded atom method (EAM) framework, ^{37,38} as described in the Methods section. Three NP ensembles cases, i.e., NS-only (Figure 3a), mixed NS-NW (Figure 3b), and

NW-only (Figure 3c) were considered. The MD simulation was successfully validated by comparing melting points, predicted using the Lindemann index,³⁹ of single Ag NSs of various diameters to past reports (Figures S4 and S5). 40,41 For computational feasibility, the NW and NS diameters in the sintering simulations were fixed at 15 nm. MD predictions showed that the melting points of individual NS and NW of this size were 1177 and 1116 K respectively, i.e., very close to the Ag bulk melting point of 1235 K expected for the 40 nm diameter nanostructures used in experiments. 41 Thus, the smaller diameters used in MD simulations here are not expected to introduce significant size-dependent meltinginduced effects on sintering. The NW length was fixed at 60 nm to capture diffusion at NW-NW and NW-NS interfaces, while avoiding the computationally difficult task of modeling a NW with micrometer length and nanometer diameter. Greater details on the MD simulations are described in the Methods section.

The ratio x/r (Figure 3d–f) at a given nanostructure interface is a key measure of neck growth ^{19,35} and also controls the interfacial junction resistivity $R_{\rm c}$. Generally, greater x/r increases the contact area at the interface between adjacent nanostructures, and the resulting increase in electron percolation pathways reduces the $R_{\rm c}$. For example, for sintered nanospheres $R_{\rm c}$ depends on x/r as per the Riemann–Weber relationship ⁴² (eq 1), where $R_{\rm solid}$ is the electrical resistivity of the bulk material. Although this formulation was developed for sintering nanospheres, our past work ⁴³ has shown that it can also be used for NW–NW interfaces.

$$R_{c} = R_{\text{solid}} \left[r \cdot x^{-1} + \pi^{-1} \cdot \ln(2r \cdot x^{-1}) \right]$$
 (1)

The evolution of x/r at different nanostructure interfaces, in Figure 4, yields the following interesting observations. First, x/

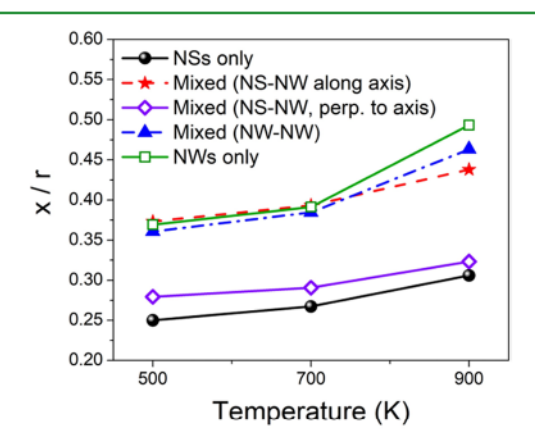


Figure 4. Average x/r at various interfaces after 300 ps of isothermal sintering.

r for the NW-only case is nearly 2 times greater than that for NS-only case. Thus, based on the Riemann–Weber formulation $R_{\rm c}$ at NW–NW interfaces is significantly lesser than that at NS–NS interfaces. Past work in isothermal sintering has posited that it is the reduction in number of interfacial contact points that reduces resistivity of NW-only films relative to NS-only films. Our above observation shows that there is an additional and significant contribution of faster neck growth at NW–NW interfaces to the lower resistivity in NW-only films. The second observation is for the mixed NW–NS ensemble. In the mixed ensemble, x/r and $R_{\rm c}$ at the NW–NS ensemble.

NW interfaces are very similar to that for the NW-only case. At the NW-NS interface, the x/r perpendicular to the NW axis is similar to that for the NS-only case, and that along the NW axis is significantly higher and similar to that for the NW-only case. This anisotropy in x/r at NW-NS interfaces has not been reported before. Since the Riemann-Weber equation has not been validated for anisotropic neck growth, we use the fact that interfacial contact area increases with x/r to understand how R_c at NW-NS interfaces compares to that at NW-NW and NS-NS interfaces. Due to the above observed anisotropy in x/r at NW-NS interfaces and the observed interfacespecific evolution of x/r, the sintered interfacial contact area depends on the interface type as NW-NW > NW-NS > NS-NS. Since increasing contact area reduces junction resistivity, the R_c at NW-NS interfaces is lower than that at NS-NS interfaces but not as low as that for NW-NW interfaces. The increased conductivity in isothermal sintering of NS-NW films as compared to NS-only films has been primarily attributed to the creation of more contiguous percolation pathways due to the introduction of NWs.²⁷ Our finding suggests that reduced R_c at NW-NS interfaces and at NW-NW interfaces plays an additional and significant role in resistivity reduction for mixed NW-NS ensembles relative to NS-only ensembles. Our observation also suggests that under isothermal sintering at the same temperature, the resistivity of NW-NS ensembles should still be higher than that of NWonly ensembles, which is in line with experimental observations from isothermal sintering.²

To identify the reasons behind the observed interfacespecific evolution of x/r, we analyzed surface and grain boundary diffusion and dislocation generation in our MD simulations. These are the neck growth mechanisms that are typically significant in sintering of nanostructures. 32,44,45 Figure S6 illustrates a representative example of motion of surface and grain boundary atoms in the MD simulations. To calculate the surface and grain boundary diffusion coefficients (D_S and D_{GR} respectively), on average 30-50 surface atoms and grain boundary atoms were chosen near the interface between adjacent nanostructures of interest. The D_S and D_{GB} , calculated using Einstein's relationship 46 as described in the Methods section, are plotted in Figure 5. The dependence of D_S on interface type is NS-NS > NS-NW > NW-NW (Figure 5a). If this surface diffusion is the dominant mechanism behind the interface-specific differences in x/r, then the x/r trends should be the opposite to that seen in Figure 4. On the other hand, the D_{GB} varies with interface type as NW-NW > NW-NS > NS-NS (Figure 5b). Since greater D_{GB} should result in greater x/r, 30 this observed dependence of D_{GB} could explain the interface-specific x/r trends in Figure 4, except for the fact that $D_{\rm GB} \approx 1/3 D_{\rm S}$, and surface diffusion dominates over grain boundary diffusion. Thus, surface and grain boundary diffusion cannot provide a complete explanation for the observed neck growth trends.

Dislocation generation at different interfaces during sintering was identified in the MD simulations, after the methodology described by Stukowski et al., 47 as described in the Methods section. During sintering, dislocation loops consisting of edge and screw dislocations are created primarily at the interparticle interfaces (Figure 6a,b). The total dislocation length $L_{\rm D}$ was calculated by adding the lengths of individual dislocation segments at a given time point and temperature combination. As time and sintering temperature increase, $L_{\rm D}$ reduces, as expected (Figure 6c-e). The general dependence of $L_{\rm D}$ on

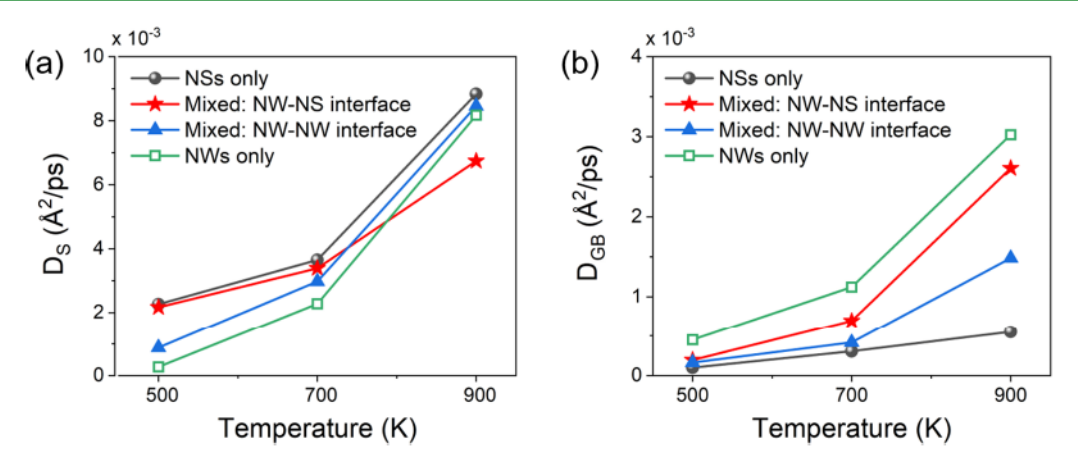


Figure 5. Coefficients for (a) surface diffusion, (b) grain boundary diffusion at different interfaces.

interface type is NW-NW > NW-NS > NS-NS, especially at 500 and 700 K (Figure 6c,d). At 900 K, the L_D values converge to a similar value (Figure 6e). In the mixed ensembles, $L_{\rm D}$ at NW-NW interfaces is greater than that in NW-only ensembles, and LD at NS-NW interfaces is greater than that at NS-NS interfaces in NS-only ensembles. Thus, the NS-NW interaction in mixed ensembles increases dislocation generation beyond those expected from NS-only and NW-only ensembles. An important observation is that the dependence of $L_{\rm D}$ on the interface type is similar to that of x/r in Figure 4. Greater dislocation generation generally increases neck growth by increasing atomic diffusion from the volume of the nanostructures⁴⁸ and by increasing the sintering stresses.⁴⁹ Since solely surface diffusion cannot explain the x/r trends, grain boundary diffusion is much smaller than surface diffusion, and dislocation generation trends are similar to the x/r trends, we conclude that dislocation-induced mass transfer is the dominant mechanism causing the observed interface-specific changes in x/r.

Thus, the answer to our first question is that neck growth in NW-NS ensembles is anisotropic and occurs at a different rate than in NW-NW and NS-NS ensembles. Changes in the dislocation-based mass transfer are primarily responsible for this phenomenon. This insight of interface-specific neck growth in sintering of mixed dissimilar-shape nanostructures is significant due to its applicability beyond IPL, to other processes like isothermal oven sintering and laser sintering.

It is worth examining the reason for interface-specific trends in these sintering mechanisms. The driving force behind surface diffusion is the effective curvature of the free surfaces, 50 i.e., of the nanostructure surfaces in contact, with greater curvature resulting in greater surface diffusion. 51,52 This surface-curvature dependence is also seen for NS-only systems where reduction in diameter increases D_s . The curvature of a NW surface is anisotropic, with only curvature around the NW axis being nonzero, as compared to a NS, which has fully isotropic curvature. As a result, the effective curvature of a NW-NW nanostructure system is lesser than that of a NW-NS interface, which is in turn lesser than that of the NS-NS interface. Thus, the driving force for surface diffusion and the D_S changes with interface type as NS-NS > NS-NW > NW-NW. Greater grain boundary diffusion during sintering is primarily due to greater interfacial stresses, either due to increased external applied pressure^{45,52} or due to increased dislocation generation.^{45,49} Since there is no external pressure applied in the MD simulations, the stress causing the observed

grain boundary diffusion here is attributable primarily to dislocation generation. The observed dependence of $L_{\rm D}$ on interface type as NW-NW > NW-NS > NS-NS and the resulting similarity in interface-specific dislocation-induced stresses qualitatively explain the similar dependence of D_{GB} on interface type. The dependence of dislocation generation on the interface type is connected to the mechanism of how dislocations are formed during nanostructure sintering. It has been shown⁴⁸ that after initial neck formation, the previously amorphous atoms on the free surface of the unsintered nanostructures, that are now in the neck region, undergo recrystallization to the bulk crystal structure (face-centered cubic for Ag here) and give rise to dislocations. Therefore, a potential source for the observed dependence of $L_{\rm D}$ on the interface type is an interface-specific change in degree of recrystallization after initial neck growth. However, further verification of this mechanism is an open question, given the potential effects of stresses from neighboring nanostructures on additional dislocation generation at the interface of interest.

3.3. Electromagnetic Simulations. To answer our second question, the unsintered and sintered ensemble morphologies were used as nanostructures with an incident electric field in finite element analysis of Maxwell's electromagnetic equations. The sintered geometries from MD simulations were directly used to account for the interfacespecific differences in neck size, unlike previous work, which assumed equal neck growth at all interfaces³⁵ or did not study mixed ensembles at all. 15,20 A unit electric field linearly polarized along direction E and traveling along direction k was incident on the nanostructure ensemble (Figure 7). The ensemble was inside a spherical air shell, surrounded by a perfectly matched layer that accommodated for spurious reflections via a scattering boundary condition (Figure S7).35 The dielectric constants of Ag were obtained from the Drude-Lorentz model.⁵⁴ Further details on the electromagnetic model are provided in the Methods section.

Figure 7 shows a representative example of the calculated thermal dissipation density contours for unsintered and sintered structures. The total thermal power dissipation $q(\lambda)$ at each wavelength λ was calculated from these contours, multiplied by the corresponding fraction of total optical irradiance, i.e., $X(\lambda)$ from the xenon lamp (Figure S1), and then divided by the volume $V_{\rm en}$ of the box enclosing each ensemble (eq 2) to obtain total thermal dissipation under IPL at λ , i.e., $Q(\lambda)$. Using $V_{\rm en}$ rather than solid volume ensured compatibility with mesoscale thermal models for IPL. ²⁰ In a

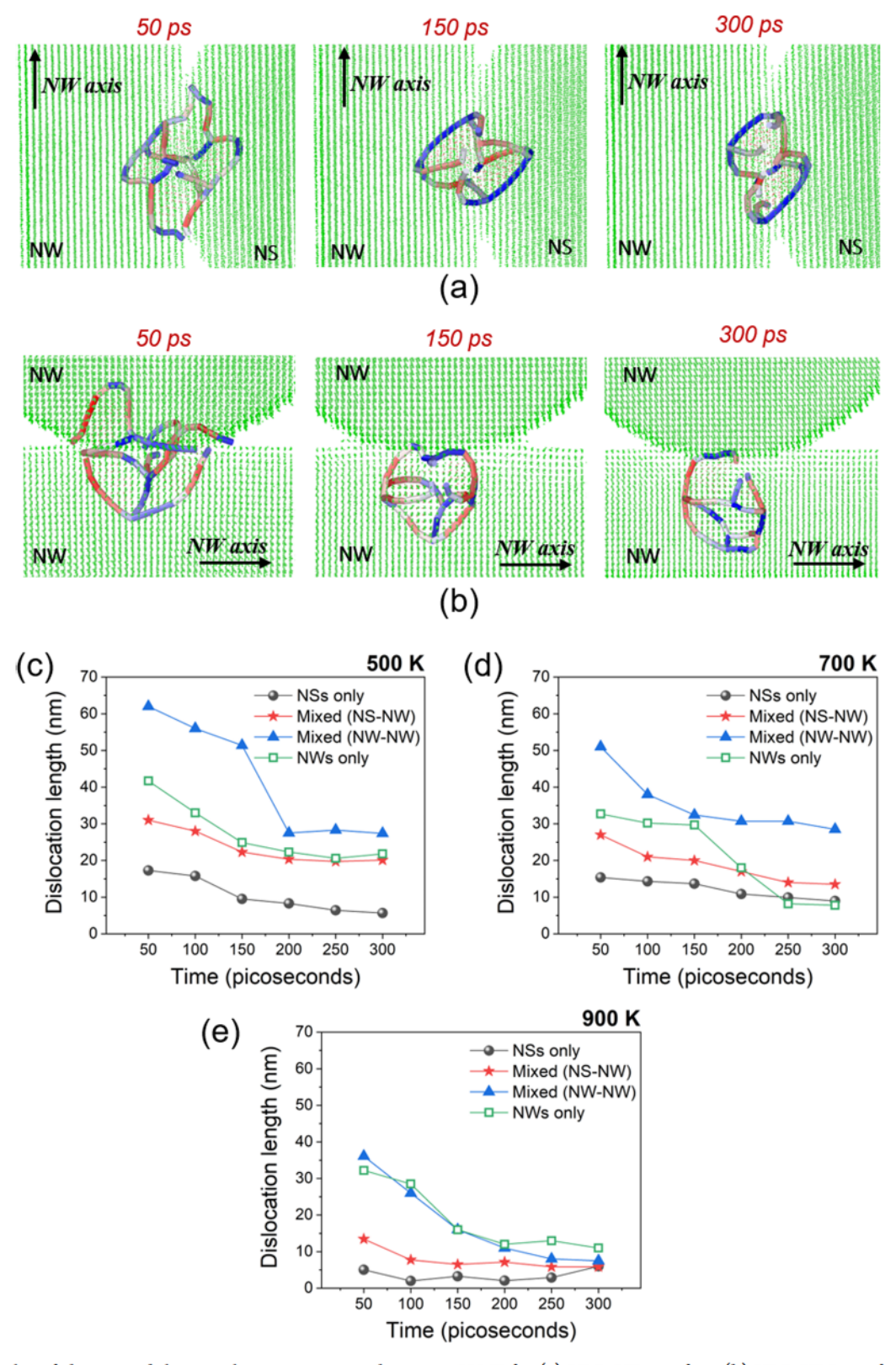


Figure 6. Examples of change in dislocation loop structures with time at 500 K for (a) NW-NS interface, (b) NW-NW interface. The red line color indicates screw character of dislocation and blue line color indicates edge character of dislocation. Evolution of dislocation length for sintering temperatures (c) 500 K, (d) 700 K, and (e) 900 K.

typical mesoscale model, heat transfer is described by a lumped capacitance approach (eq S3) due to the low Biot number of the film, ^{19,20} and effective medium approximations are used to describe the heat capacity. So, thermal power dissipation per

unit enclosed volume of film is used in this approach if the inplane and thickness of the film are known. Figure S8 shows how $Q(\lambda)$ evolves with greater sintering temperatures, which correspond to greater x/r and lower junction resistivity.

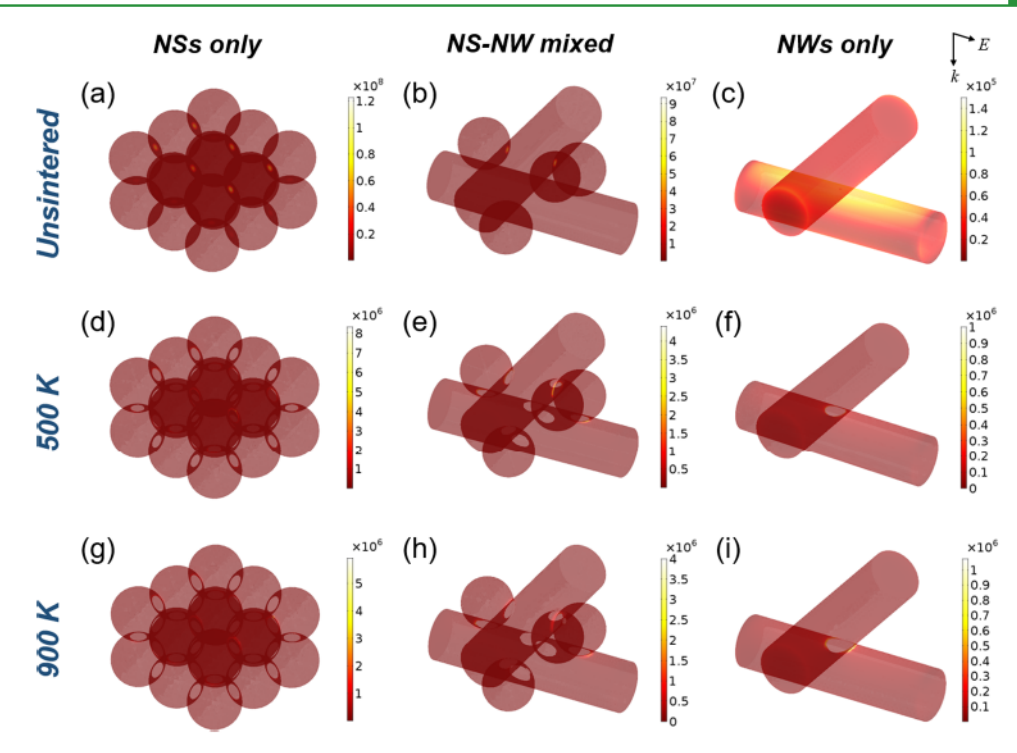


Figure 7. Contours of thermal power dissipation (W/m^3) at 450 nm under a unit incident electric field. (a-c) Unsintered nanostructure ensembles, (d-f) ensembles sintered at 500 K (g-i), ensembles sintered at 900 K.

$$Q(\lambda) = q(\lambda) \cdot X(\lambda) / V_{\rm en} \tag{2}$$

The $Q(\lambda)$ was summed over the energetic spectrum of the xenon lamp to obtain the total dissipated thermal power $Q_{\rm T}$. Figure 8 plots $Q_{\rm T}$ against average x/r in each ensemble, leading

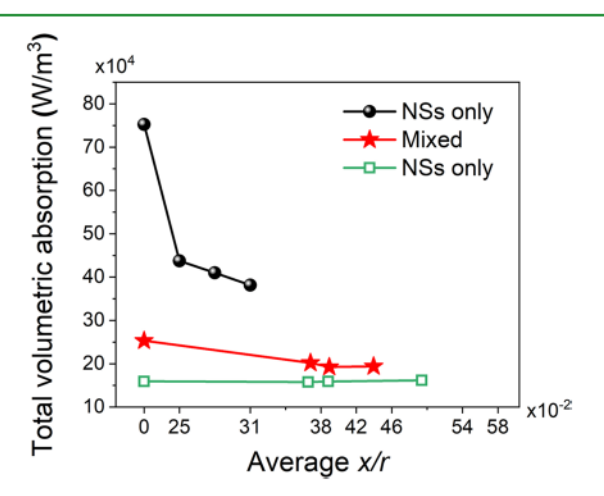


Figure 8. Change in total thermal power dissipated per unit enclosed volume of the ensemble as a function of (x/r). Shown for incident irradiance of 1 W/m^2 .

to the following observations. The NS-only curve exhibits a significant reduction in $Q_{\rm T}$ upon initial neck growth, and this reduction levels off with increasing neck growth beyond a point (e.g., $x/r \approx 0.25$ here). This trend for NS-only films agrees with past work²⁰ and with the rapid drop and then leveling off in temperatures after the first pulse in Figure 2b. In comparison, in the mixed ensemble case, the reduction in $Q_{\rm T}$ with increasing x/r is lower, and the leveling off in $Q_{\rm T}$ is reached at a higher x/r (≈ 0.39 here). Thus, the negative feedback of neck growth on $Q_{\rm T}$ in NS-only ensembles is

significantly mitigated by the introduction of NWs in the mixed NW–NS case. This observation also agrees with the experimental temperature evolution in Figure 2b, where the addition of NWs to NSs progressively reduces the temperature drop after the first pulse. For the NW-only case, the $Q_{\rm T}$ changes very little with x/r, again agreeing with temperature observations in Figure 2b, which show a fairly constant peak pulse temperature for the NW-only films. Overall, for the NS-only case, the percentage change in $Q_{\rm T}$ per unit change in x/r is 164%, a significantly larger change as compared to those for the mixed ensemble (54%) and NW-only (3%) cases.

We further note that at the same x/r, the magnitude of $Q_{\rm T}$ reduces with increasing NW content, indicating a reduced optical absorption efficiency. These observations yield the answer to our second question. The introduction of NWs into a NS ensemble mitigates the negative feedback effect of neck growth on optical absorption in IPL and simultaneously reduces absorption efficiency. Thus, adding NWs to a NS ensemble enables more sustained temperatures during IPL, but the accompanying reduced optical absorption nullifies this advantage if NW content is increased beyond a certain point. This is the reason behind the existence of an optimum NW content (50:50 mixing ratio) in our experiments as well.

3. CONCLUSIONS

This work combines experiments, mass transfer simulations, and electromagnetic simulations to understand how neck growth kinetics during sintering and self-damping optical behavior in IPL is affected by the nanostructure shape (specifically NWs and NSs here). The following is the major findings. Neck growth kinetics at Ag NW–NS interfaces is substantially anisotropic, greater than that at NW–NW interfaces, and lesser than that at NS–NS interfaces. The dominant mechanism behind this difference is an interface-specific change in dislocation generation during sintering. This

insight uncovers the non-negligible role played by mismatch in nanostructure shape on junction resistivity and overall film resistivity. The addition of NWs to a NS ensemble inherently reduces self-damping behavior and optical absorption efficiency in IPL, with the following implications for design of NW-NS films. Too high NS content causes stronger selfdamping behavior along with lesser neck growth rate, which limits the optical absorption capacity before low enough resistivity is reached. Excessive NW content reduces optical absorption efficiency to such an extent that it overwhelms the accompanying advantages of increased neck growth kinetics and more sustained optical absorption. Mixing NWs and NSs in an optimal ratio (50:50 here) reaches a balance between neck growth kinetics, optical absorption efficiency, and sustained temperature in multiple pulses. We note that one approach for using greater NW content would be to increase the incident pulse irradiance, to offset the reduced optical absorption efficiency while retaining lesser self-damping and greater neck growth. However, there is also a material cost factor to be considered since NWs are generally more expensive than NSs.

These insights constitute a set of physical phenomena to guide the choice of dissimilarly shaped nanostructures (beyond NWs and NSs⁵⁵) that should be mixed to concurrently reduce resistivity and temperatures in IPL. The ideal nanostructure shapes to be mixed should concurrently reduce self-damping, increase or retain high optical absorption efficiency, and increase or retain similar levels of neck growth rates as the unmixed nanostructures. Further, the insight on neck growth kinetics between dissimilar nanostructure shapes is applicable for designing shape composition in sintering processes beyond IPL as well. Although our work cannot determine the optimal ratio, in which to mix dissimilar-shape nanostructures, this will be possible using larger scale molecular dynamics and optical simulations that are increasingly being developed. This work also raises open questions on the exact reasons for interfacespecific dislocation generation and whether there is an underlying shape descriptor for mixed nanostructures that describes the dependence of self-damping on nanostructure shape and relative nanostructure size. Efforts to find such a shape descriptor can play a significant role in not just IPL but also in understanding the optical behavior of sintered mixedshape nanostructures.

4. METHODS

- **4.1. Experimental Methods.** Ag NSs and NWs were mixed in ethanol in a total concentration by weight of 5%. The aerosol jet printing parameters used are described in our previous work,³⁵ and the films were dried at room temperature for 5 min after printing. The IPL experiments were performed at ambient temperature. At least five experiments were conducted for each NW/NS ratio. The film thickness, IPL temperatures, film resistivity, morphology, crystallinity, and optical absorption were measured as described in our previous work.³⁵
- 4.2. Molecular Dynamics Methods. The embedded atom method (EAM),³⁷ with potential functions from Mishin et al.,⁵⁶ was used here. The Ag NSs consisted of 110 400 atoms, and Ag NWs consisted of 665 288 atoms. All initial distances between the two interfaces were set as 1 A°, within the EAM interaction cut-off distance. The simulations were performed in the LAMMPS software⁵⁷ with the Nosé–Hoover thermostat for temperature control. The nanostructures were subjected to a uniform temperature by ignoring heat transfer effects. A time step of 5 ps was chosen since it was validated to conserve energy well. The diffusion coefficients were

calculated by choosing surface and grain boundary atoms close to the desired interfaces and using Einstein's relationship 46 which is given by

$$D = \frac{1 \text{ d}}{6N \text{ d}t} \sum [r_i(t_0 + \tau) - r_i(t_0)]^2$$
 (3)

In eq 3, N is the number of atoms, t_0 is the time origin, τ is the observation time, $r(t_0)$ is atom position at time origin, and \sum represents summation over the chosen number of atoms N over all time origins. Here, τ is the simulation time of 300 ps and t_0 is at the beginning of the simulation. On average, the number of atoms N was 30–50 for calculation of both surfaces and grain boundary diffusion coefficients. The MD model was successfully validated by comparing the melting points for single Ag NS of various diameters to that from literature, as described in the Supporting Information in Discussion S4 and Figures S4 and S5. Further, the melting points for a single NS and NW, calculated using the above method, were found to be 1177 and 1116 K. Therefore, the MD simulation temperatures were below the nanostructure's melting point and within the bounds of solid-state sintering.

Identification of dislocations in sintered structures was performed using the dislocation analysis method after Stukowski et al., ⁴⁷ as implemented in the open-source OVITO software. In this method, dislocations are identified by mapping atomic bonds from the dislocated interface to an ideal template configuration to find dislocation-induced displacements and concurrently determine the dislocation's Burgers vector. The input crystal type for this analysis was face-centered cubic, corresponding to the crystal structure of Ag, and the dislocations were represented as screw and edge dislocations, as shown in Figure 6a,b.

2.3. Electromagnetic Simulations. The simulations were performed in the COMSOL software. The ensemble morphologies predicted by MD simulations were used as the nanostructure ensemble geometries in electromagnetic simulations. The electric field polarization was perpendicular to the axis of the top NW. This maximized the degree of coupling of the electromagnetic field into the ensemble. The mesh sizes and geometric parameters of the air shell and the perfectly matched layer were refined till convergence in the predicted absorption curves was obtained (Figure S7). The simulations were conducted over the 400–700 nm wavelength range, in increments of 25 nm, since this is the spectrum over which most of the xenon lamp energy lies.

ASSOCIATED CONTENT

Supporting Information

The Supporting Information is available free of charge on the ACS Publications website at DOI: 10.1021/acsami.8b17644.

Power spectrum of light from xenon lamp, Figure S1; temperature evolution curves for Ag films, Figure S2; optical absorption spectrum of Ag nanomaterial films, Figure S3; melting point analysis, Figures S4 and S5, equations S1 and S2; atomic motions of surface and grain boundary atoms during sintering, Figure S6; electromagnetic model, Figure S7; optical absorption from electromagnetic simulations, Figure S8; thermal equation, equation S3 (PDF)

AUTHOR INFORMATION

Corresponding Author

*E-mail: rajiv.malhotra@rutgers.edu. Tel: +1-848-445-5058. Fax: +1-732-445-3124.

ORCID

Hyun-Jun Hwang: 0000-0002-2152-2540

Notes

The authors declare no competing financial interest.

ACKNOWLEDGMENTS

This work was supported by the National Science Foundation, United States, grants CMMI #1809289 and CBET #1449383.

REFERENCES

- (1) Kamyshny, A.; Magdassi, S. Conductive Nanomaterials for Printed Electronics. Small 2014, 10, 3515-3535.
- (2) Magdassi, S.; Bassa, A.; Vinetsky, Y.; Kamyshny, A. Silver Nanoparticles as Pigments for Water-based Ink-jet Inks. *Chem. Mater.* 2003, 15, 2208–2217.
- (3) Kang, J.; Ryu, J.; Kim, H.; Hahn, H. Sintering of Inkjet-Printed Silver Nanoparticles at Room Temperature using Intense Pulsed Light. *J. Electron. Mater.* 2011, 40, 2268–2277.
- (4) Chung, W.-H.; Hwang, H.-J.; Lee, S.-H.; Kim, H.-S. In situ Monitoring of a Flash Light Sintering Process using Silver Nano-Ink for Producing Flexible Electronics. *Nanotechnology* 2012, 24, No. 035202.
- (5) Hu, L.; Choi, J. W.; Yang, Y.; Jeong, S.; La Mantia, F.; Cui, L.-F.; Cui, Y. Highly Conductive Paper for Energy-Storage Devices. *Proc. Natl. Acad. Sci. U.S.A.* 2009, 106, 21490–21494.
- (6) Hoth, C. N.; Choulis, S. A.; Schilinsky, P.; Brabec, C. J. High Photovoltaic Performance of Inkjet Printed Polymer: Fullerene Blends. Adv. Mater. 2007, 19, 3973—3978.
- (7) Krebs, F. C.; Tromholt, T.; Jørgensen, M. Upscaling of Polymer Solar Cell Fabrication using Full Roll-to-Roll Processing. *Nanoscale* 2010, 2, 873–886.
- (8) Sirringhaus, H.; Kawase, T.; Friend, R.; Shimoda, T.; Inbasekaran, M.; Wu, W.; Woo, E. High-Resolution Inkjet Printing of All-Polymer Transistor Circuits. *Science* 2000, 290, 2123–2126.
- (9) Subramanian, V.; Fréchet, J. M.; Chang, P. C.; Huang, D. C.; Lee, J. B.; Molesa, S. E.; Murphy, A. R.; Redinger, D. R.; Volkman, S. K. Progress toward Development of All-Printed RFID Tags: Materials, Processes, and Devices. *Proc. IEEE* 2005, 93, 1330–1338.
- (10) Russo, A.; Ahn, B. Y.; Adams, J. J.; Duoss, E. B.; Bernhard, J. T.; Lewis, J. A. Pen-on-Paper Flexible Electronics. *Adv. Mater.* 2011, 23, 3426–3430.
- (11) Chen, P.; Chen, H.; Qiu, J.; Zhou, C. Inkjet Printing of Single-Walled Carbon Nanotube/RuO₂ Nanowire Supercapacitors on Cloth Fabrics and Flexible Substrates. *Nano Res.* 2010, 3, 594–603.
- (12) Van Osch, T. H.; Perelaer, J.; de Laat, A. W.; Schubert, U. S. Inkjet Printing of Narrow Conductive Tracks on Untreated Polymeric Substrates. *Adv. Mater.* 2008, 20, 343–345.
- (13) Perelaer, J.; Smith, P. J.; Mager, D.; Soltman, D.; Volkman, S. K.; Subramanian, V.; Korvink, J. G.; Schubert, U. S. Printed Electronics: the Challenges Involved in Printing Devices, Interconnects, and Contacts based on Inorganic Materials. *J. Mater. Chem.* 2010, 20, 8446–8453.
- (14) Hwang, H.-J.; Joo, S.-J.; Kim, H.-S. Copper Nanoparticle/ Multiwalled Carbon Nanotube Composite Films with High Electrical Conductivity and Fatigue Resistance Fabricated via Flash Light Sintering. ACS Appl. Mater. Interfaces 2015, 7, 25413—25423.
- (15) Garnett, E. C.; Cai, W.; Cha, J. J.; Mahmood, F.; Connor, S. T.; Christoforo, M. G.; Cui, Y.; McGehee, M. D.; Brongersma, M. L. Self-limited Plasmonic Welding of Silver Nanowire Junctions. *Nat. Mater.* 2012, 11, 241–249.
- (16) Wang, B.-Y.; Yoo, T.-H.; Song, Y.-W.; Lim, D.-S.; Oh, Y.-J. Cu Ion Ink for a Flexible Substrate and Highly Conductive Patterning by Intensive Pulsed Light Sintering. ACS Appl. Mater. Interfaces 2013, 5, 4113–4119.
- (17) Dharmadasa, R.; Jha, M.; Amos, D. A.; Druffel, T. Room Temperature Synthesis of a Copper Ink for the Intense Pulsed Light Sintering of Conductive Copper Films. ACS Appl. Mater. Interfaces 2013, 5, 13227–13234.
- (18) Kang, H.; Sowade, E.; Baumann, R. R. Direct Intense Pulsed Light Sintering of Inkjet-Printed Copper Oxide Layers within Six Milliseconds. ACS Appl. Mater. Interfaces 2014, 6, 1682–1687.

- (19) MacNeill, W.; Choi, C.-H.; Chang, C.-H.; Malhotra, R. On the Self-Damping Nature of Densification in Photonic Sintering of Nanoparticles. *Sci. Rep.* 2015, *5*, No. 14845.
- (20) Bansal, S.; Malhotra, R. Nanoscale-Shape-Mediated Coupling between Temperature and Densification in Intense Pulsed Light Sintering. *Nanotechnology* 2016, 27, No. 495602.
- (21) Song, C.-H.; Han, C. J.; Ju, B.-K.; Kim, J.-W. Photoenhanced Patterning of Metal Nanowire Networks for Fabrication of Ultraflexible Transparent Devices. ACS Appl. Mater. Interfaces 2016, 8, 480–489.
- (22) Yim, C.; Sandwell, A.; Park, S. S. Hybrid Copper—Silver Conductive Tracks for Enhanced Oxidation Resistance under Flash Light Sintering. ACS Appl. Mater. Interfaces 2016, 8, 22369—22373.
- (23) Yim, C.; Kockerbeck, Z. A.; Jo, S. B.; Park, S. S. Hybrid Copper—Silver—Graphene Nanoplatelet Conductive Inks on PDMS for Oxidation Resistance Under Intensive Pulsed Light. ACS Appl. Mater. Interfaces 2017, 9, 37160—37165.
- (24) Jang, Y.-R.; Chung, W.-H.; Hwang, Y.-T.; Hwang, H.-J.; Kim, S.-H.; Kim, H.-S. Selective Wavelength Plasmonic Flash Light Welding of Silver Nanowires for Transparent Electrodes with High Conductivity. ACS Appl. Mater. Interfaces 2018, 10, 24099–24107.
- (25) Kim, H.-S.; Dhage, S. R.; Shim, D.-E.; Hahn, H. T. Intense Pulsed Light Sintering of Copper Nanoink for Printed Electronics. *Appl. Phys. A* 2009, 97, 791–798.
- (26) Joo, S.-J.; Park, S.-H.; Moon, C.-J.; Kim, H.-S. A Highly Reliable Copper Nanowire/Nanoparticle Ink Pattern with High Conductivity on Flexible Substrate Prepared via a Flash Light-Sintering Technique. ACS Appl. Mater. Interfaces 2015, 7, 5674—5684.
- (27) Stewart, I. E.; Kim, M. J.; Wiley, B. J. Effect of Morphology on the Electrical Resistivity of Silver Nanostructure Films. ACS Appl. Mater. Interfaces 2017, 9, 1870–1876.
- (28) Bergin, S. M.; Chen, Y.-H.; Rathmell, A. R.; Charbonneau, P.; Li, Z.-Y.; Wiley, B. J. The Effect of Nanowire Length and Diameter on the Properties of Transparent, Conducting Nanowire Films. *Nanoscale* 2012, 4, 1996–2004.
- (29) Mutiso, R. M.; Sherrott, M. C.; Rathmell, A. R.; Wiley, B. J.; Winey, K. I. Integrating Simulations and Experiments to Predict Sheet Resistance and Optical Transmittance in Nanowire Films for Transparent Conductors. *ACS Nano* 2013, 7, 7654–7663.
- (30) Castro, R. Modelling "Nano-Effects" in Sintering. In Sintering. Mechanisms of Convention Nanodensification and Field Assisted Processes; Ricardo, H. R. C.; van Benthem, K., Eds.; Springer, 2013; Chapter 2, pp 17–34.
- (31) Ding, L.; Davidchack, R. L.; Pan, J. A Molecular Dynamics Study of Sintering between Nanoparticles. *Comput. Mater. Sci.* 2009, 45, 247–256.
- (32) Song, P.; Wen, D. Molecular Dynamics Simulation of the Sintering of Metallic Nanoparticles. *J. Nanopart. Res.* **2010**, *12*, 823–829
- (33) Wang, J.; Shin, S.; Hu, A. Geometrical Effects on Sintering Dynamics of Cu-Ag Core-Shell Nanoparticles. *J. Phys. Chem. C* 2016, 120, 17791–17800.
- (34) Koparde, V. N.; Cummings, P. T. Molecular Dynamics Simulation of Titanium Dioxide Nanoparticle Sintering. *J. Phys. Chem.* B 2005, 109, 24280–24287.
- (35) Dexter, M.; Bhandari, R.; Chang, C.; Malhotra, R. Controlling Processing Temperatures and Self-Limiting Behaviour in Intense Pulsed Sintering by Tailoring Nanomaterial Shape Distribution. *RSC Adv.* 2017, 7, 56395–56405.
- (36) Su, K. H.; Wei, Q. H.; Zhang, X.; Mock, J. J.; Smith, D. R.; Schultz, S. Interparticle Coupling Effects on Plasmon Resonances of Nanogold Particles. *Nano Lett.* 2003, 3, 1087–1090.
- (37) Daw, M. S.; Baskes, M. I. Embedded-Atom Method: Derivation and Application to Impurities, Surfaces, and Other Defects in Metals. *Phys. Rev. B* 1984, 29, 6443–6453.
- (38) Foiles, S. Application of the Embedded-Atom Method to Liquid Transition Metals. *Phys. Rev. B* 1985, 32, 3409-3415.

- (39) Neyts, E. C.; Bogaerts, A. Numerical Study of the Size-Dependent Melting Mechanisms of Nickel Nanoclusters. *J. Phys. Chem. C* 2009, *113*, 2771–2776.
- (40) Shi, F. G. Size Dependent Thermal Vibrations and Melting in Nanocrystals. *J. Mater. Res.* 1994, *9*, 1307–1314.
- (41) Alarifi, H. A.; Atis, M.; Ozdogan, C.; Hu, A.; Yavuz, M.; Zhou, Y. Determination of Complete Melting and Surface Premelting Points of Silver Nanoparticles by Molecular Dynamics Simulation. *J. Phys. Chem. C* 2013, *117*, 12289–12298.
- (42) Zhang, Y.; Wu, L.; Guo, X.; Jung, Y.-G.; Zhang, J. Molecular Dynamics Simulation of Electrical Resistivity in Sintering Process of Nanoparticle Silver Inks. *Comput. Mater. Sci.* 2016, 125, 105–109.
- (43) Michael, D.; Andrew, P.; Zhongwei, G.; Gregory, S. H.; Chihhung, C.; Rajiv, M. Modeling Nanoscale Temperature Gradients and Conductivity Evolution in Pulsed Light Sintering of Silver Nanowire Networks. *Nanotechnology* 2018, 29, No. 505205.
- (44) Yang, L.; Gan, Y.; Zhang, Y.; Chen, J. K. Molecular Dynamics Simulation of Neck Growth in Laser Sintering of Different-sized Gold Nanoparticles under Different Heating Rates. *Appl. Phys. A* 2012, 106, 725–735.
- (45) Cheng, B.; Ngan, A. H. W. The Sintering and Densification Behaviour of Many Copper Nanoparticles: A Molecular Dynamics Study. *Comput. Mater. Sci.* 2013, 74, 1–11.
- (46) Keffer, D. J.; Adhangale, P. The Composition Dependence of Self and Transport Diffusivities from Molecular Dynamics Simulations. *Chem. Eng. J.* 2004, 100, 51–69.
- (47) Stukowski, A.; Vasily, V. B.; Athanasios, A. Automated Identification and Indexing of Dislocations in Crystal Interfaces. *Model. Simul. Mater. Sci. Eng.* 2012, 20, No. 085007.
- (48) Seong, Y.; Kim, Y.; German, R.; Kim, S.; Kim, S.-G.; Kim, S. J.; Kim, H. J.; Park, S. J. Dominant Mechanisms of the Sintering of Copper Nano-Powders Depending on the Crystal Misalignment. *Comput. Mater. Sci.* 2016, 123, 164–175.
- (49) Wang, F.; Tang, Z.; He, H. Stress-Dislocation Interaction Mechanism in Low-Temperature Thermo-Compression Sintering of Ag NPs. AIP Adv. 2018, 8, No. 045012.
- (50) Searcy, A. W. Driving Force for Sintering of Particles with Anisotropic Surface Energies. J. Am. Ceram. Soc. 1985, 68, C-267-C-268
- (51) Mullins, W. W. Theory of Thermal Grooving. J. Appl. Phys. 1957, 28, 333-339.
- (52) Wakai, F.; Brakke, K. A. Mechanics of Sintering for Coupled Grain Boundary and Surface Diffusion. *Acta Mater.* 2011, *59*, 5379–5387.
- (53) Jiang, Q.; Zhang, S. H.; Li, J. C. Grain Size-dependent Diffusion Activation Energy in Nanomaterials. *Solid State Commun.* 2004, 130, 581–584.
- (54) Fan, X.; Zheng, W.; Singh, D. J. Light Scattering and Surface Plasmons on Small Spherical Particles. *Light Sci. Appl.* 2014, 3, No. e179.
- (55) Kinnear, C.; Moore, T. L.; Rodriguez-Lorenzo, L.; Rothen-Rutishauser, B.; Petri-Fink, A. Form Follows Function: Nanoparticle Shape and Its Implications for Nanomedicine. *Chem. Rev.* 2017, 117, 11476–11521.
- (56) Mishin, Y.; Farkas, D.; Mehl, M.; Papaconstantopoulos, D. Interatomic Potentials for Monoatomic Metals from Experimental Data and ab initio Calculations. *Phys. Rev. B* 1999, 59, No. 3393.
- (57) Plimpton, S. Fast Parallel Algorithms for Short-range Molecular Dynamics. J. Comput. Phys. 1995, 117, 1–19.